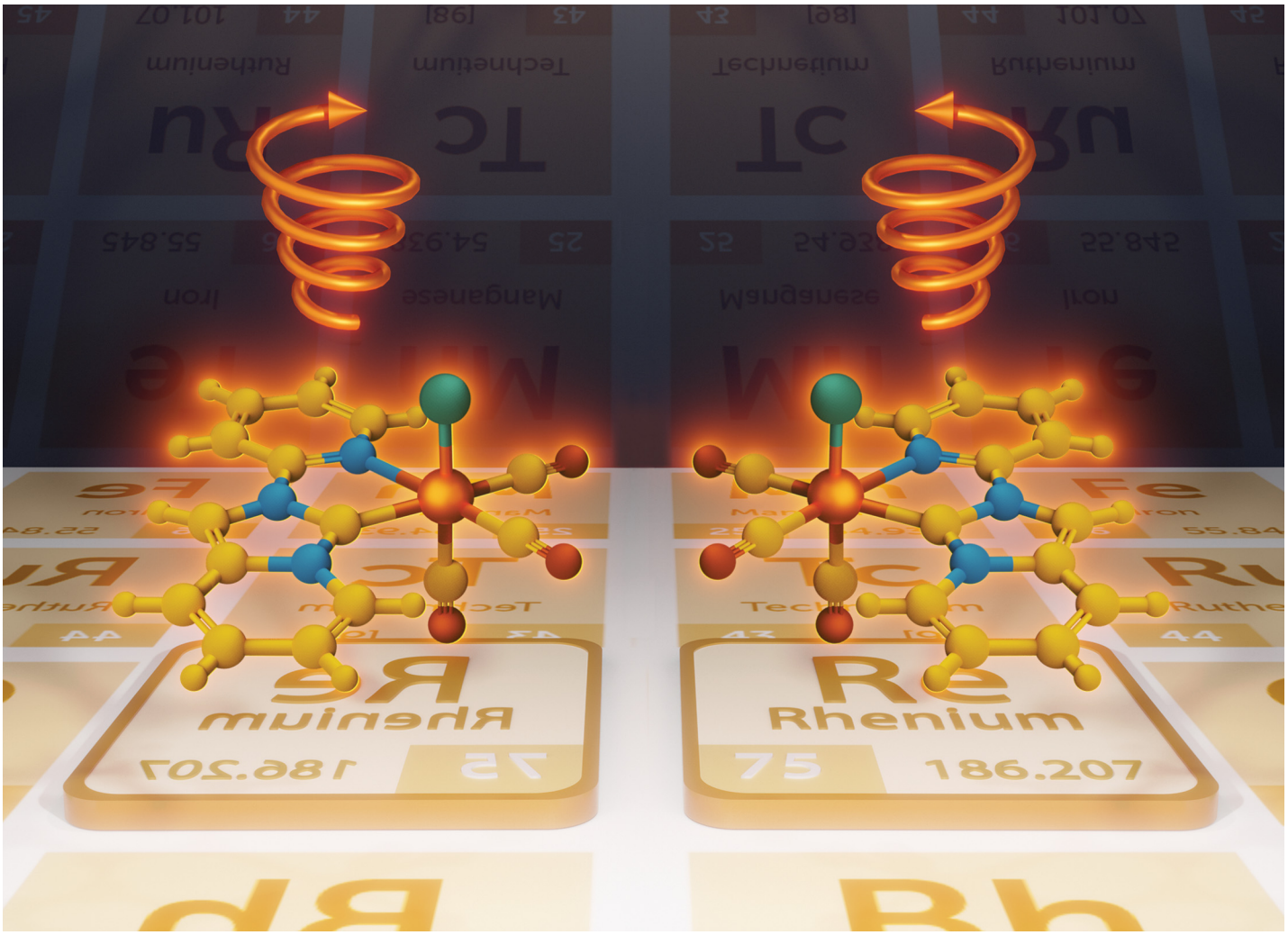

Showcasing research of Dr Matteo Mauro, Dr Jeanne Crassous and Dr Chantal Daniel's laboratories, CNRS, Universities of Strasbourg and Rennes, France

Chiroptical activity of benzannulated N-heterocyclic carbene rhenium(I) tricarbonyl halide complexes: towards efficient circularly polarized luminescence emitters

The computed and experimental (chiro-)optical properties of a series of eight enantiopure phosphorescent N-heterocyclic carbene rhenium(I) tricarbonyl complexes are compared in terms of ECD and CPL activities. The study deciphers the effect exerted by the nature of the low-lying electronic excited states onto the chiro-optical properties, paving the way to the design of enantiomerically pure circularly polarized luminescent CPL emitters.

Jurga Valanciunaite, Scientific Illustrator (www.jv-science-illustration.fr), is acknowledged for the cover artist view.

Periodic table reproduced with permission from the Royal Society of Chemistry

As featured in:

See Jeanne Crassous, Chantal Daniel, Matteo Mauro *et al.*, *Phys. Chem. Chem. Phys.*, 2024, **26**, 4855.

ROYAL SOCIETY OF CHEMISTRY

rsc.li/pccp

Registered charity number: 207890

PCCP Owner Societies

PCCP

PAPER

View Article Online
View Journal | View Issue

Check for updates

Cite this: *Phys. Chem. Chem. Phys.*, 2024, **26**, 4855

Chiroptical activity of benzannulated N-heterocyclic carbene rhenium(I) tricarbonyl halide complexes: towards efficient circularly polarized luminescence emitters†

Valerio Giuso,[a] Christophe Gourlaouen,[b] Mathias Delporte--Pébay,[c] Thomas Groizard,[b] Nicolas Vanthuyne,[d] Jeanne Crassous,*[c] Chantal Daniel*[b] and Matteo Mauro*[a]

Received 5th September 2023,
Accepted 9th November 2023

DOI: 10.1039/d3cp04300b

rsc.li/pccp

Published on 14 November 2023. Downloaded on 11/20/2025 6:23:24 PM.

The design of enantiomerically pure circularly polarized luminescent (CPL) emitters would enormously benefit from the accurate and in-depth interpretation of the chiroptical properties by means of jointly (chiroptical) photophysical measurements and state-of-the-art theoretical investigation. Herein, computed and experimental (chiro-)optical properties of a series of eight enantiopure phosphorescent rhenium(I) tricarbonyl complexes are systematically compared in terms of electronic circular dichroism (ECD) and CPL. The compounds have general formula *fac*-[ReX(CO)$_3$(N^C$_{NHC}$)], where N^C$_{NHC}$ is a pyridyl benzannulated N-heterocyclic carbene deriving from a (substituted) 2-(pyridin-2-yl)imidazo[1,5-*a*]pyridin-2-ium proligand and X = Cl, Br and I, and display structured red phosphorescence with long-lived (τ = 7.0–19.1 μs) excited-state lifetime and dissymmetry factors $|g_{Lum}|$ up to 4×10^{-3}. The mixing of the character of the lowest-lying emitting triplet excited state is finely modulated between ligand centred (^{3}LC), metal-to-ligand charge transfer (^{3}MLCT) and halogen-to-ligand charge transfer (^{3}XLCT) by the nature of the ancillary halogen and the chromophoric N^C$_{NHC}$ ligand. The study unravels the effect exerted by the nature of the excited state onto the ECD and CPL activity and will help to pave the way to construct efficient CPL emitters by chemical design.

1 Introduction

Understanding the interplay between the electronic and structural parameters that govern chiroptical properties such as electronic circular dichroism (ECD) and circularly polarized luminescence (CPL), is of primary importance for the rational design of robust and efficient CP-active molecules.[1–4] The establishment of structure-chiroptical properties relationships is therefore a pivotal key-enabling step towards the design of efficient CPL emitters with enhanced chiroptical response suitable for emerging technological applications, such as circularly polarized organic light-emitting diodes (CP-OLEDs), bio-imaging probes and chiral detectors.[5,6] Several efforts are currently underway to unknot such fundamental understanding, yet this is far from being an easy task. This achievement becomes even more challenging in the case of transition metal complexes that possess richer excited state features and that are characterized by admixing of states with different character as well as spin–orbit coupling (SOC) and spin–vibronic (SVC) coupling.[7–9]

N-heterocyclic carbenes (NHCs) are a unique class of ligands that find widespread application in organometallic chemistry.[10–12] They demonstrated to be of particular interest and suitable for pushing quenching metal centered (^{3}MC) excited states up to higher energies, and enabled preparation of robust and highly-emissive transition metal complexes (TMCs).[13] In this framework, Crassous and co-workers investigated the chiroptical activity of enantiopure *tris*-carbonyl Re–NHC complexes (**I-II**), along with the novel longer-lived counterparts bearing the N-(pyridyl)-[5]helicene-imidazolylidene (**III**),[14] and *N*-(aza[6]helicenyl)-benzimidazolylidene (**IV**)[15] helicenic–NHC scaffold as depicted in Scheme 1. A detailed theoretical investigation based on accurate spin–orbit calculations has enabled us to reproduce the experimental CPL spectra and to assign the CPL activity of a series of

[a] Université de Strasbourg, CNRS Institut de Physique et Chimie des Matériaux de Strasbourg, UMR 7504 23 rue du Loess, 67034 Strasbourg, France. E-mail: mauro@unistra.fr
[b] Laboratoire de Chimie Quantique Université de Strasbourg CNRS UMR7177 Institut Le Bel 4 Rue Blaise Pascal, 67000 Strasbourg, France. E-mail: c.daniel@unistra.fr
[c] Université de Rennes, CNRS, ISCR – UMR 6226, 35000 Rennes, France. E-mail: jeanne.crassous@univ-rennes1.fr
[d] Aix Marseille University, CNRS Centrale Marseille, iSm2, 13284 Marseille, France

† Electronic supplementary information (ESI) available. See DOI: https://doi.org/10.1039/d3cp04300b

Published on 14 November 2023. Downloaded on 11/20/2025 6:23:24 PM.

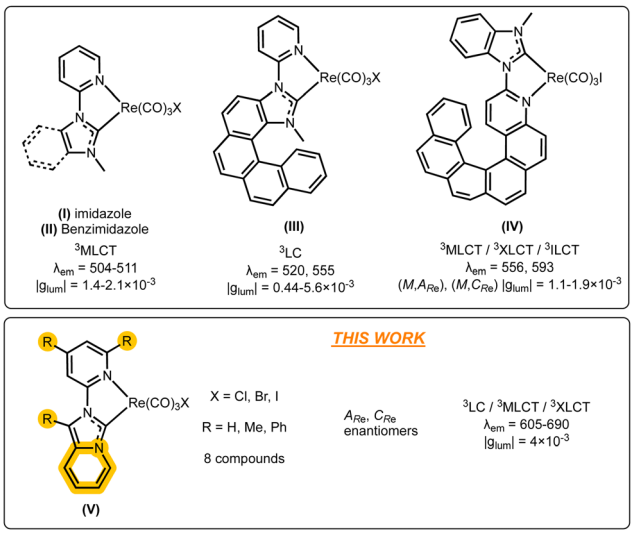

Scheme 1 Selected examples of tricarbonyl Re(I)–NHC halide complexes investigated in the field of chiroptics.

$[ReX(CO)_3(N^\wedge C_{NHC})]$ (X = Cl or I; $N^\wedge C_{NHC}$ = 1-(2-pyridyl)-4-methyl-imidazole, 1-(2-pyridyl)-4-methyl-benzimidazole and 1-(2-pyridyl)-2[4]-helicene-4-methyl-imidazole) complexes as well as to understand the correlation between electronic density character and spin density polarization that control the CPL activity in this class of molecules.[16] On these grounds, it appears that the sizeable triplet ligand centred (^{3}LC) nature of the emissive excited state localized onto the chiral ligand is of importance for achieving good CPL phosphorescence in such class of emitters (Scheme 1). Helicenic ligands have provided complexes with interesting chiroptical activities to date. Nevertheless, enlarging the structural diversity will help to better understand the influence of electronic and structural parameters on the CPL activities in chiral luminescent complexes. It would also be of interest to use ligands made *via* more straightforward synthetic protocols.[14]

Recently, Mauro and co-workers reported on a novel family of luminescent rhenium(I) complexes bearing a pyridyl pyridoannelated NHC ligand with ^{3}LC emission, belonging to the family of general formula (**V**) in Scheme 1.[17]

Stemming from our long-standing interest in the photophysics and photochemistry of rhenium(I) tricarbonyl complexes as well as NHC-based emitters for optoelectronics,[18–24] we questioned whether the use of a less extended, yet benzannulated, NHC scaffold with a limited steric demand would be suitable for the construction of efficient CPL-active phosphorescent rhenium(I)-based emitters. Therefore, the purpose of the present study is to explore the effect exerted by different substituents onto the photophysical and chiroptical properties of a family of enantiopure $[ReX(CO)_3(N^\wedge C_{NHC})]$ complexes, where N^C is a benzannulated NHC deriving from a series of six (substituted) 2-(pyridin-2-yl)imidazo[1,5-*a*]pyridin-2-ium pro-ligands (Schemes 1 and 2).

The objective is to subtly modify the ligand to obtain a suitable mixing of LC_{NHC}/MLCT/XLCT character in the lowest-lying triplet-manifold excited states. Proper character mixing

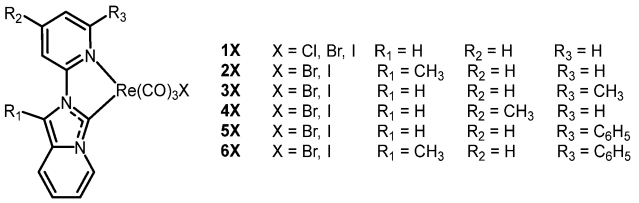

Scheme 2 Chemical structure of the *fac*-rhenium(I) tricarbonyl complexes **1Cl**, **1Br**, **1I**, **2Br-6Br** and **2I-6I** herein investigated.

will be advantageous for achieving visible light absorption, efficient luminescence and CPL activity. Indeed, MLCT character of the emitting excited state is of great importance for achieving efficient radiative relaxation and outstanding emission performances,[25] whereas ^{3}LC character is expected to be beneficial for intense chiroptical activity.[16] We present here a systematic modeling and interpretation of absorption, emission, ECD and CPL properties of the investigated complexes aiming at developing a rational design of new and efficient phosphorescent CPL emitters.

2 Results and discussion

2.1. Modeling and theoretical interpretation

Guided by a computationally-driven molecular design approach, this section is dedicated to the theoretical study of a whole series of benzannulated NHC rhenium(I) tricarbonyl complexes belonging to class (**V**). Their chemical structure and corresponding name are displayed in Scheme 2. Among these, halo-derivatives **1Cl**, **1Br**, **1I** as well as bromo derivatives **2Br-6Br** were also prepared and further investigated experimentally (*vide infra*).

Our aim is not to determine accurate vibronic spectra for a direct comparison with highly resolved experimental absorption and/or ECD spectra,[16,26,27] but to select the most promising molecules on the basis of the electronic and structural properties of their excited states prior to an experimental validation. All the calculations are based on Kohn–Sham density functional theory (KS-DFT) including solvent and SOC corrections. The computational details are provided in the experimental Section.

2.1.1. Structural and electronic properties. To shed a better light on the electronic and chiroptical properties on this series of luminescent Re complexes, electronic ground state structures were fully optimized as A_{Re}/C_{Re} enantiomers for all the complexes (Fig. S1 of the ESI†). At this stage it should be pointed out that numerical error may be the cause of negligible distortion of the expected mirror image structures. Introduction of a methyl group on the chromophoric pyridyl–NHC scaffold (**2Br**, **3Br** and **4Br**) gives rise to minor structural changes compared to the unsubstituted benchmark complex **1Br**, independently of the position of the methyl onto either the pyridyl or the NHC moiety. Substitution of the pyridyl moiety by a phenyl (**5Br** and **6Br**) adds some geometrical flexibility due to

 This journal is © the Owner Societies 2024

Published on 14 November 2023. Downloaded on 11/20/2025 6:23:24 PM.

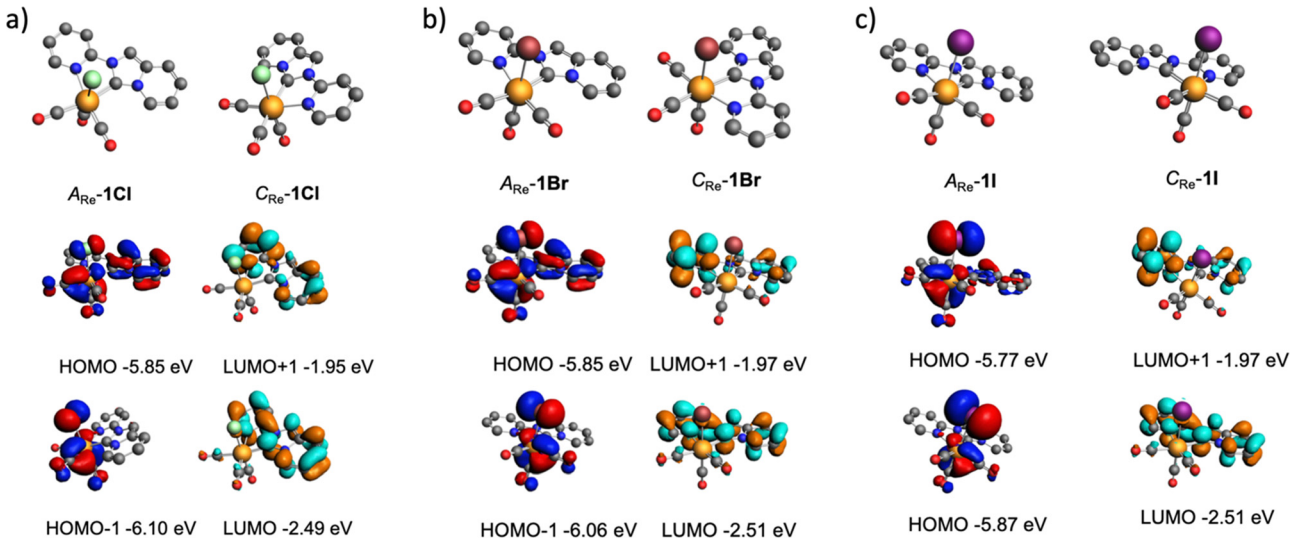

Fig. 1 Optimized structures and Kohn–Sham FMO plots computed for derivative **1Cl** (a), **1Br** (b) and **1I** (c) with A_{Re} (left) and C_{Re} (right) stereochemistry.

possible rotation of the phenyl ring about the $C_{pyridine}$–C_{phenyl} bond.

The homologous series **1X** (where X = Cl, Br and I) was investigated in order to ascertain the effect exerted by halogen substitution. The Kohn–Sham Frontier Molecular Orbitals (KS FMOs) are displayed in Fig. 1. As far as HOMO level is concerned, halide character increases when going from **1Cl** to **1Br** to **1I**, expectedly, and this is accompanied by a destabilization of the HOMO energy by 80 meV in the iodo complex **1I** compared to chlorido **1Cl** and the bromido **1Br** counterparts. This change in character will have important consequences on the nature of the lower-lying excited states and spin–orbit effects (see below).

As expected, the LUMO character remains largely unaffected by the change of the axial halide. This overall trend is common for all the investigated complexes. The corresponding FMOs along with their energies are depicted in Fig. S2–S6 of the ESI.† Introduction of a methyl group onto the N^C_{NHC} ligand yields to a destabilization of both the HOMO and the LUMO level, although the former is affected to a much larger extent. This destabilization is particularly significant when the substitution is made on the NHC core (**2Br-2I** *vs.* **3Br-4I**). Larger destabilization of both the HOMO and LUMO occurs in compound **6Br** due to the concomitant methyl substitution at the NHC site and phenyl substitution of the pyridyl moiety. Phenyl substitution on the pyridyl ring in α position to the coordinated nitrogen (**5Br-6Br**) affects the frontier orbital to a minor extent. In all complexes the HOMO remains delocalized over the NHC ligand and to a lesser extent on the metal atom with very weak contributions of the halide and of the carbonyls, whereas the LUMO is delocalized on the benzannulated–NHC ligand leading to a very similar picture in term of qualitative description of the electronic structures.

2.1.2. Absorption and ECD spectra. The following section discusses solvent and substitution effects on the absorption and ECD spectroscopy exerted by the modification of the halide ligand and NHC scaffold. Most of the calculations were performed in both toluene and acetone in order to provide a coherent benchmarking for further experiments, which can be potentially perturbed by practical constraints in specific solvents (*e.g.* solubility).

Halogen effect. The absorption spectra of the A_{Re} conformation of the benchmark series of complex **1**, (A_{Re})-**1Cl**, (A_{Re})-**1Br** and (A_{Re})-**1I**, are displayed in Fig. 2 and were computed including SOC effect. The transition energies, oscillator strengths, absorption wavelengths calculated with SOC are reported in Table 1 for **1Cl**, **1Br** and **1I** and in Table S1–S2 of the ESI† for the other complexes.

As far as compound **1Cl** and **1Br** are concerned, the computed absorption spectra start at 540 nm and involve the population of the lowest triplet T_1 of LC_{NHC} character by SO effects (see Table 1). Both complexes possess a set of four bands between 470 and 420 nm with significant singlet contributions and oscillator strengths of the order of 10^{-2}. Moving from Cl to

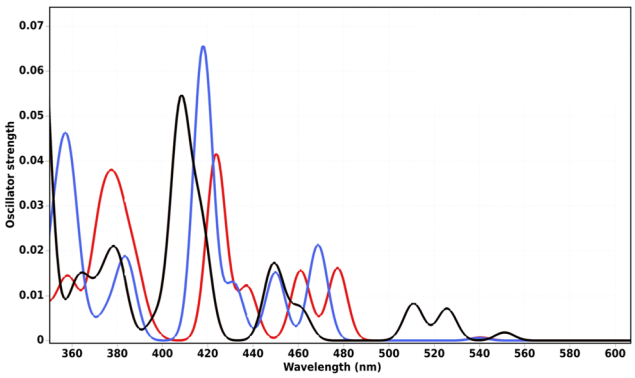

Fig. 2 Absorption spectra of compound **1Cl** (blue), **1Br** (red) and **1I** (black) calculated as A_{Re} chiral-at-rhenium configuration and computed by TD-DFT including SOC in toluene as the solvent.

Published on 14 November 2023. Downloaded on 11/20/2025 6:23:24 PM.

Br to I yields an increase of the halide-to-ligand-charge-transfer (XLCT) character of the lower-lying electronic transitions.

As expected, the introduction of iodide as the ancillary ligand bathochromically shifts the absorption onset due to SOC effect that increases the triplet contribution in the lowest band. The absorption of compound **1I** starts at 550 nm with an electronic transition from ground to the lowest "spin–orbit" excited state with nearly pure triplet LC_{NHC} character. The first shoulder at 526 nm, composed of S_1 (43%) and T_2 (36%) is followed by bands of weak intensities at 511 nm and 461 nm corresponding to mixing between $T_3/S_2/T_2$ and $S_1/T_2/T_3$, respectively. The first intense band is calculated at 448 nm and is composed of S_2 (53%) and T_3 (15%). As illustrated by the electronic transition characters computed at Franck–Condon without SOC, S_1 has a mainly XLCT character as well as T_2 and T_3 (see Fig. 3). On the other hand, T_1 remains purely LC_{NHC} in nature and localized on the pyridyl-NHC ligand. At higher energy, the iodo complex **1I** is characterized by a high density of "spin–orbit" states between 526 and 448 nm with three bands corresponding to S_1/T_2, $S_2/T_2/T_3$ and S_2/T_3 mixed states. These bands are less intense than the corresponding states in **1Cl** and **1Br** (Fig. 2) because of a decrease of the singlet character in **1I** due to spin–orbit effects (Table 1).

The computed ECD spectra calculated without SOC and based on the contribution of each singlet absorbing state are depicted in Fig. 4 and the data listed in Table 2 for **1Cl**, **1Br** and **1I**. The intensity of the signal, given by the rotatory strengths, depends on the LC_{NHC} contribution in the singlet states. Indeed, as recently demonstrated for similar complexes $[ReX(CO)_3L]$ (L = 1-(2-pyridyl)-4-methyl-benzimidazole); (X = Cl, I)[16] the LC or ILCT transitions are in principle π–π* *z*-polarized and consequently electric dipole "forbidden" and magnetic dipole "allowed". Since the electronic, structural and optical properties of **1Cl** and **1Br** appear to be very similar, only **1Br** and **1I** complexes are selected for further investigation that includes SOC.

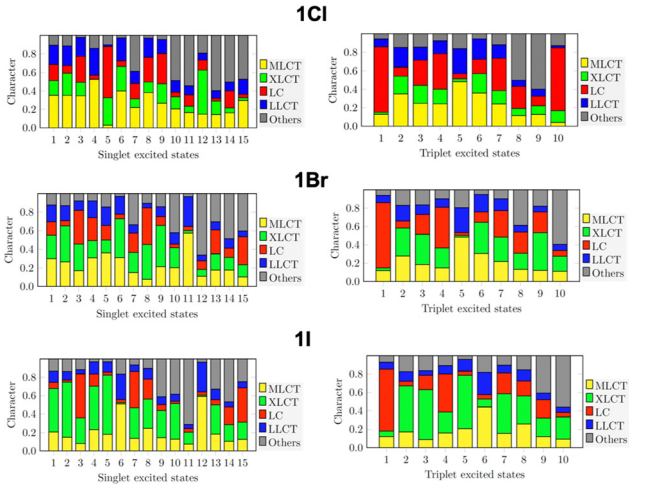

Fig. 3 Character of the electronic transition at Franck–Condon without SOC in toluene which are associated to the low-lying singlet and triplet excited states computed for compound **1Cl**, **1Br** and **1I** with A_{Re} conformation. (Others include localized MC and CT to the carbonyl group).

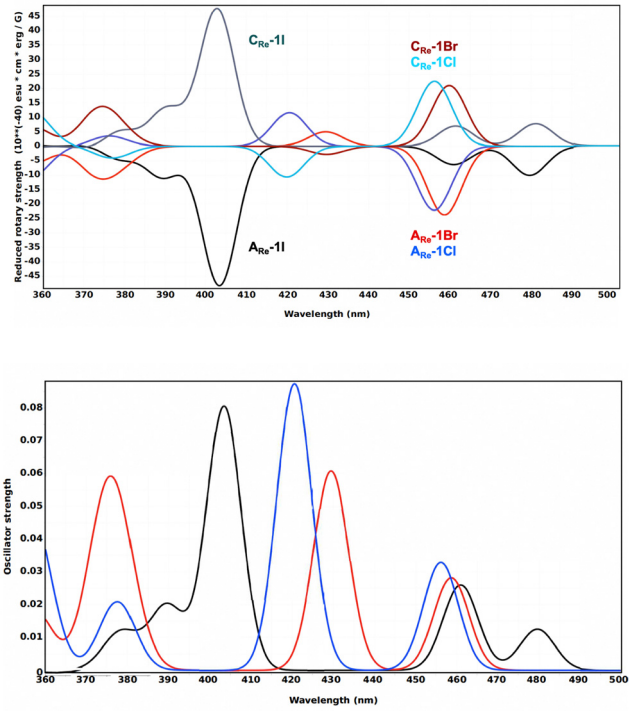

Fig. 4 Calculated TD-DFT absorption (bottom) and ECD (top) without SOC for compounds **1Cl** (blue), **1Br** (red) and **1I** (black) ECD-calculated as A_{Re} and C_{Re} chiral-at-rhenium configurations in toluene as the solvent.

The significant LC_{NHC} contribution to the S_3 state in **1I** leads to the most intense computed ECD signal at 403 nm within the series. The ECD spectrum of **1Br** calculated with SOC (Fig. S7 of the ESI†) does not exhibit significant differences as compared to the one obtained without SOC providing a qualitatively similar picture (Fig. 4). The first band is slightly red-shifted by SOC (459 *vs.* 477 nm) and is unambiguously attributed to state E_4 (Fig. 4 and Table 1), the three components of the triplet state E_1, E_2 and E_3 having no intensities. The band computed at λ = 438 nm is due to the "spin–orbit" state E_8. Both states originate from the scalar singlet state S_1 coupled with triplet states T_2 and T_3 and keep their MLCT/XLCT character.

Ligand substituent effects. The absorption spectra for A_{Re} enantiomers of **2Br**, **2I**, **6Br** and **6I** computed by TD-DFT including SOC are depicted in Fig. 5 together with the spectra of the reference complexes **1Br** and **1I**, respectively. The absorption spectra of the investigated Re(I) complexes and computed with and without SOC are depicted in Fig. S8–S13 of the ESI.†

Independently of the halide, substitution at either the imidazo[1,5-*a*]pyridilydene core (*i.e.* **2Br** and **2I**) or at both the NHC and the pyridyl moiety (*i.e.* **6Br** and **6I**) leads to a small bathochromic shift of the lower energy side of the absorption spectrum. This effect can be attributed to the electron enrichment of the HOMO, slightly destabilized by around 0.1–0.2 eV due to the presence of the moderately electron-donating methyl group(s). The calculated spectra of A_{Re} enantiomers of derivative **2Br-2I** and **6Br-6I** also show a small bathochromic shift of the higher-energy bands by methyl substitution, in an energy

 This journal is © the Owner Societies 2024

Published on 14 November 2023. Downloaded on 11/20/2025 6:23:24 PM.

Table 1 Transition energies, associated wavelengths and oscillator strengths of the low-lying singlet, triplet and "spin–orbit" states of compounds **1Cl**, **1Br** and **1I** computed as A_{Re} enantiomer in toluene

1Cl	Transition energy [eV]	Wavelength [nm]	f	**1Cl**	Transition energy [eV]
Singlet				Triplet	
S_1	2.72	456	0.33×10^{-1}	T_1	2.30
S_2	2.95	421	0.87×10^{-1}	T_2	2.77
S_3	3.28	378	0.18×10^{-1}	T_3	2.87
S_4	3.31	375	0.25×10^{-2}	T_4	3.23
S_5	3.46	358	0.34×10^{-1}	T_5	3.27
				T_6	3.42
				T_7	3.47

1Cl	Transition energy [eV]	Wavelength [nm]	f	Composition[a]
Spin–orbit states				
E_1	2.30	540	0.72×10^{-5}	T_1
E_2	2.30	540	0.12×10^{-4}	T_1
E_3	2.30	540	0.58×10^{-3}	T_1
E_4	**2.65**	**469**	**0.21×10^{-1}**	**64% $S_1$27% T_2**
E_5	2.71	457	0.12×10^{-4}	74% T_2 20% T_3
E_6	2.72	457	0.13×10^{-3}	75% T_2 20% T_3
E_7	**2.76**	**450**	**0.15×10^{-1}**	**35% T_2 16% S_1 11% S_2**
E_8	**2.87**	**432**	**0.13×10^{-1}**	**61% T_3 18% S_1**
E_9	2.90	428	0.13×10^{-4}	48% T_3 18% T_2
E_{10}	2.90	428	0.10×10^{-3}	T_3
E_{11}	**2.97**	**418**	**0.66×10^{-1}**	**75% S_2 10% T_3**
E_{12}	3.20	387	0.62×10^{-4}	T_4
E_{13}	3.20	387	0.35×10^{-3}	T_4
E_{14}	3.21	386	0.27×10^{-2}	T_4
E_{15}	**3.23**	**383**	**0.15×10^{-1}**	**79% S_3**

1Br	Transition energy [eV]	Wavelength [nm]	f	**1Br**	Transition energy [eV]
Singlet				Triplet	
S_1	2.70	459	0.28×10^{-1}	T_1	2.30
S_2	2.89	429	0.61×10^{-1}	T_2	2.73
S_3	3.26	381	0.12×10^{-1}	T_3	2.81
S_4	3.30	376	0.42×10^{-1}	T_4	3.17
S_5	3.33	372	0.17×10^{-1}	T_5	3.28
				T_6	3.39

1Br	Transition energy [eV]	Wavelength [nm]	f	Composition[a]
Spin–orbit states				
E_1	2.29	541	0.32×10^{-4}	T_1
E_2	2.29	541	0.74×10^{-4}	T_1
E_3	2.29	540	0.59×10^{-3}	T_1
E_4	**2.60**	**477**	**0.16×10^{-1}**	**55% S_1 27% T2**
E_5	2.64	469	0.13×10^{-4}	T2/T_3
E_6	265	569	0.48×10^{-3}	T2/T_3
E_7	**2.69**	**461**	**0.15×10^{-1}**	**26% T_2 22% T_3 21% S_2**
E_8	**2.83**	**438**	**0.11×10^{-1}**	**35% T_3 30% S_1 16% T_2**
E_9	2.86	433	0.22×10^{-4}	T3/T_2
E_{10}	2.87	433	0.12×10^{-2}	T3/T_2
E_{11}	**2.93**	**424**	**0.42×10^{-1}**	**68% S_2 15% T_3**

1I	Transition energy [eV]	Wavelength [nm]	f	**1I**	Transition energy [eV]
Singlet				Triplet	
S_1	2.59	480	0.12×10^{-1}	T_1	2.29
S_2	2.69	461	0.26×10^{-1}	T_2	2.58
S_3	3.07	403	0.80×10^{-1}	T_3	2.62
S_4	3.18	390	0.20×10^{-1}	T_4	3.07
S_5	3.28	378	0.11×10^{-1}	T_5	3.23
				T_6	3.27
				T_7	3.29

1I	Transition energy [eV]	Wavelength [nm]	f	Composition[a]
Spin–orbit states				
E_1	2.24	553	0.17×10^{-4}	T_1
E_2	2.24	553	0.12×10^{-3}	T_1
E_3	2.25	551	0.17×10^{-2}	T_1
E_4	**2.36**	**526**	**0.71×10^{-2}**	**43% S_1 36% T_2**
E_5	2.40	517	0.16×10^{-4}	T_2/T_3

Published on 14 November 2023. Downloaded on 11/20/2025 6:23:24 PM.

Table 1 (*continued*)

1Cl	Transition energy [eV]	Wavelength [nm]	f	**1Cl**	Transition energy [eV]
E_6	2.40	517	0.85×10^{-4}		T_2/T_3
E_7	**2.43**	**511**	**0.83×10^{-2}**		**29% T_3 28% S_2 12% T_2**
E_8	**2.69**	**461**	**0.69×10^{-2}**		**26% S_1 19% T_3 26% T_2**
E_9	2.72	456	0.22×10^{-4}		T_3/T_2
E_{10}	2.74	452	0.44×10^{-2}		T_3/T_2
E_{11}	**2.76**	**448**	**0.14×10^{-1}**		**53% S_2 15% T_3**

[a] Composition of the "spin–orbit" states in term of low-lying singlet and triplet excited states calculated without SOC.

Table 2 Reduced rotatory strengths R (in 10^{-40} esu cm erg G^{-1}), magnetic transition dipole x, y, z components (in a.u.) and associated singlet excited states computed for compounds (A_{Re})-**1Cl**, (A_{Re})-**1Br** and (A_{Re})-**1I**

Compound		R [10^{-40} esu cm erg G^{-1}]	m_x	m_y	m_z	State character
(A_{Re})-**1Cl**	S_1	−22.10	0.04	−0.000084	−0.56	MLCT/LLCT/XLCT
	S_2	11.58	−0.15	−0.017	0.0035	MLCT/LLCT/XLCT
	S_3	1.71	−0.049	0.106	0.37	MLCT/LC/LLCT
(A_{Re})-**1Br**	S_1	−23.71	−0.0019	0.032	−0.50	MLCT/XLCT
	S_2	4.95	−0.17	0.0063	−0.013	XLCT/MLCT
	S_3	−2.78	−0.032	0.082	0.10	LC/XLCT/MLCT
(A_{Re})-**1I**	S_1	−10.76	−0.028	0.026	−0.33	XLCT/MLCT
	S_2	−6.36	−0.073	0.053	−0.019	XLCT
	S_3	**−48.22**	**0.010**	**0.12**	**0.56**	**LC/XLCT**

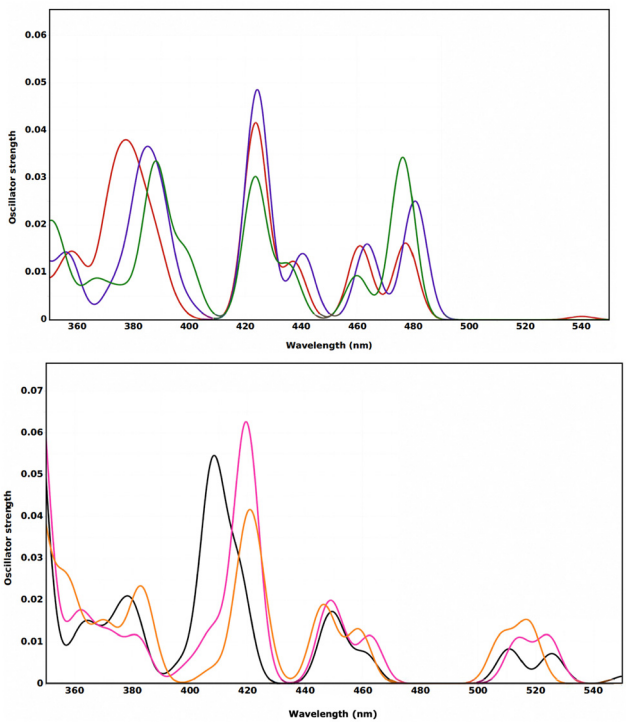

Fig. 5 Calculated electronic absorption spectra of **1Br** (red), **2Br** (purple), **6Br** (green) (top) and **1I** (black), **2I** (magenta), **6I** (orange) (bottom) in toluene with SOC.

domain where LC and LLCT transitions provide the major contributions to the absorption (Fig. 5).

The transition energies of the lower-lying singlet, triplet and "spin–orbit" (SO) states along with the corresponding transition wavelengths and oscillator strengths are listed in Tables S2 and S3 of the ESI† for all investigated bromido and iodo complexes, respectively. The character of the corresponding transitions at Franck–Condon (FC) is obtained by means of TheoDORE analysis in Fig. S14–S18 of the ESI.†

Almost no effect is observed for compounds **5Br-5I** while there is a small hypsochromic shift for the first states in **4Br-4I** and **3Br-3I** as compared to **1Br-1I**. Remarkably, when substituting the pyridyl moiety in the complexes **4Br-4I** and **3Br-3I**, the ECD signal generated by the S_3 state at about 400 nm increases slightly as compared to the reference complex (Table S3 of the ESI†). This is due to an increase in LC character of the corresponding transition. This effect is more pronounced in the case of the iodo complex **1I** as illustrated in Fig. 6. It should be pointed out that no change of sign of the reduced rotatory strength is observed for the complex **1I** within the 360–500 nm window (Fig. 6) while a change

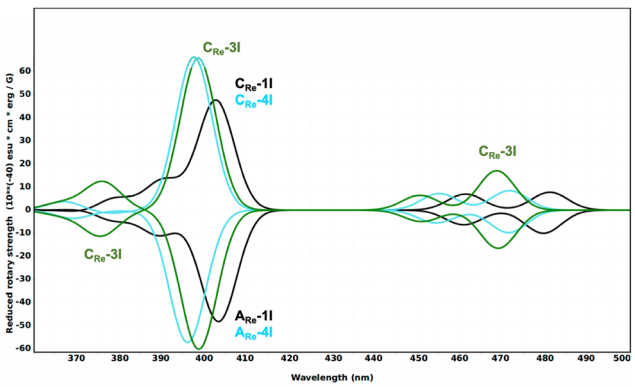

Fig. 6 Calculated ECD spectra of derivative **1I** (black), **3I** (green) and **4I** (cyan) as both A_{Re} and C_{Re} enantiomers without SOC in toluene. (Remarkably, no change of sign of the reduced rotatory strength is observed for the complexe **1I** within the 360–500 nm window).

 This journal is © the Owner Societies 2024

Published on 14 November 2023. Downloaded on 11/20/2025 6:23:24 PM.

of sign is observed at 376 nm for the complex **3I** and to a less extend **4I**. This is correlated to the nearly pure XLCT character of the S5 absorbing state of **1I** (Fig. 3), less ECD active than the XLCT/MLCT transitions S_4 that contribute to this band in **3I** and **4I** (Fig. S15 and S16 of the ESI†).

For all investigated complexes, the reduced rotatory strengths, the magnetic transition dipole *x*, *y*, *z* components and associated singlet excited states are reported in Table S3 of the ESI.† The corresponding ECD spectra are displayed in Fig. S19–S23 of the ESI.† Both S_1 and S_3 possess enough LC character to produce a modest signal at about 470–450 nm and 420–400 nm.

A comparison between the ECD activities of the present molecules and the complexes $[ReI(CO)_3L]$ (L = 1-(2-pyridyl)-4-methyl-imidazole and 1-(2-pyridyl)-2[4]-helicene-4-methyl-imidazole) complexes investigated both experimentally[14] and theoretically[16] indicates a drastic bathochromic shift of the signal. Indeed, both complexes of series (**II**) and (**III**) do not show any signal below 390 nm with a very weak ECD activity between 340–390 nm for the NHC one. The huge ECD activity of the helicenic complex starts at 330 nm (reduced rotatory strength $>100 \times 10^{-40}$ esu cm erg G^{-1}) with the presence of nearly pure LC transitions in the upper singlet excited states involving the helicene–NHC scaffold ($LC_{NHC-hel}$).

Solvent effect. Further computational analysis was carried out in acetone to investigate the effect of the change in environment polarity on the chiroptical properties. Indeed, moving to more polar solvent, such as acetone, has negligible effects on the shape of the absorption spectra, as illustrated in Fig. 7, where the computed absorption and ECD spectra of (A_{Re})-**1Br** in toluene and acetone are compared. Calculated transition energies increase by 0.2–0.3 eV in acetone compared to toluene and, as consequence, the lowest part of the absorption spectrum displays an overall hypsochromic shift in acetone (Table S4 of the ESI† and Fig. 7). A noticeable exception appears for T_1 and its spin–orbit sub-levels for which the hypsochromic shift is as small as *ca.* 0.05 eV. This difference arises from its LC character, compared to the other states for which the MLCT contribution is more important. The small hypsochromic shift of T_1 in more polar solvent is attributed to the variation in molecular dipolar moment going from S_0 to T_1. The latter state is less polar than the former as illustrated for example by the computed dipole moment in **1Br**, being μ = 15.3 D *vs.* 15.7 D in the excited and ground state, respectively, computed in acetone.

The hypsochromic shift of the absorption spectra observed in acetone is reflected in the ECD spectra (Fig. 7). In addition, larger rotatory strengths are obtained in acetone (Table S5 of the ESI†). This effect could be related to the change of the dipolar moment since a more polar solvent, such as acetone, will induce sizable fluctuations favourable to higher rotatory strengths.

2.1.3. Emissive properties and CPL activity. The emissive properties of the investigated Re(I) complexes are analyzed on the basis of the optimized structures of the low-lying triplet excited states. The electronic properties and energetics of the low-lying excited states computed without SOC in toluene and acetone are reported in Table 3 and Table S6 of the ESI,†

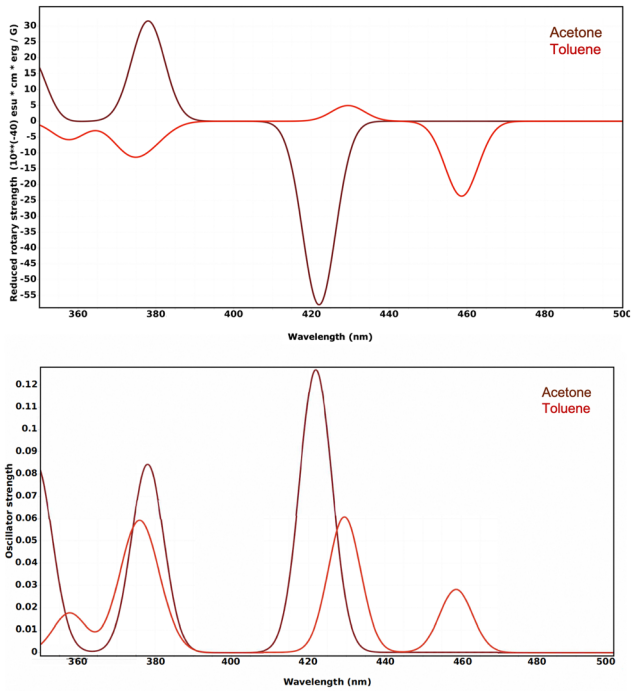

Fig. 7 Calculated absorption spectra (bottom) and ECD spectra (top) of (A_{Re})-**1Br** in acetone (dark garnet) and toluene (red) as the solvent (without SOC).

respectively. The calculated stabilization and deformation energies are defined in Scheme 3. For the T_1 state of the complexes reported in Table 3, of nearly pure LC_{NHC} character at Franck–Condon, the stabilization and deformation energies are between 1.91–2.18 eV and 0.31–0.50 eV, respectively. This state leads to a lowest emission ranging from 730 nm to 780 nm. In all complexes the T_1 state loses its pure $^3LC_{NHC}$ character to gain a mixed state either with ^{3}MLCT, ^{3}XLCT or admixed ^{3}MLCT/^{3}XLCT nature upon relaxation. The second calculated band ranging between 620 nm and 600 nm is originated from the XLCT, MLCT or XLCT/MLCT transitions at FC and acquires a XMLCT or MXLCT character associated to deformation energies between 0.34 and 0.48 eV and stabilization energies between 2.41 and 2.53 eV.

Optimization of the T_4 excited state, not accessible for all molecules, especially when the ligand flexibility increases, leads to an important stabilization of this LC_{NHC} containing transition. The stabilization reaches 3.02 eV (**1Br**) and 2.88 eV (**1I**) and is accompanied by a significant deformation of 1.04 eV (**1Br**) and 0.94 eV (**1I**), yielding a band at 626 nm and 642 nm, respectively. The calculated emission wavelengths (Table 3) cover the whole range (600–780 nm) of the vibronically structured emission spectra discussed in the experimental section. The solvent has negligible effect on emission properties (Table 3 and Table S6 of the ESI†). We observe a very small blue shift of emission wavelength in acetone as compared to toluene. This blue shift can be linked to the nature of the T_1 state which has a dominant ^{3}LC character and that is less polar than the S_0 ground state as discussed above for the absorption. A similar picture is observed in all complexes.

Published on 14 November 2023. Downloaded on 11/20/2025 6:23:24 PM.

Table 3 Transition energies at Franck–Condon (FC), emission energies (in eV) and wavelengths (in nm), character at Frank–Condon and at the triplet optimized structure, deformation (E_{def}) and stabilization (E_{stab}) energies (in eV) of the lowest triplet states of complexes **1Cl**, **1Br**, **1I**, **2Br**, **3Br**, **4Br**, **5Br**, **6Br** as A_{Re} enantiomers in toluene. The definitions of E_{def} and E_{stab} are given in Scheme 3

	FC [eV]	FC character	Emission energy [eV]	Emission wavelength [nm]	Optimized structure character	E_{def} [eV]	E_{stab} [eV]
1Cl							
T_1	2.30	LC	1.68	738	LC/MLCT/XLCT	0.32	2.00
T_2	2.77	MLCT/LLCT/XLCT	2.04	608	MXLCT	0.43	2.47
T_3	2.87	LC/MLCT/XLCT	1.98	626	MXL CT	0.73	2.71
1Br							
T_1	2.30	LC	1.68	738	MXLCT/LC	0.50	2.18
T_2	2.73	XMLCT	2.06	602	MXLCT	0.41	2.47
T_3	2.80	XMLCT	2.02	614	MXLCT	0.65	2.67
T_4	3.17	LC/XLCT	1.98	626	LC/MLCT	1.04	3.02
1I							
T_1	2.29	LC	1.68	738	XMLCT/LC	0.31	1.99
T_2	2.58	XLCT	2.06	602	XMLCT	0.34	2.41
T_3	2.62	MXLCT	2.06	602	XLCT	0.46	2.52
T_4	3.07	LC/XLCT	1.93	642	MLCT/LC	0.94	2.88
2Br							
T_1	2.22	LC	1.60	775	MXLCT/LC	0.31	1.91
T_2	2.72	MXLCT	2.00	620	MXLCT	0.48	2.48
3Br							
T_1	2.32	LC	1.70	729	MXLCT/LC	0.32	2.02
T_2	2.79	MXLCT	2.06	602	MXLCT	0.47	2.53
4Br							
T_1	2.32	LC	1.69	734	MXLCT	0.32	2.01
T_2	2.76	MXLCT	2.06	602	MXLCT	0.44	2.50
5Br							
T_1	2.31	LC	1.68	738	MXLCT/LC	0.33	2.01
T_2	2.77	XMLCT	2.05	605	MXLCT	0.44	2.49
6Br							
T_1	2.23	LC	1.60	775	LC/MLCT	0.33	1.93

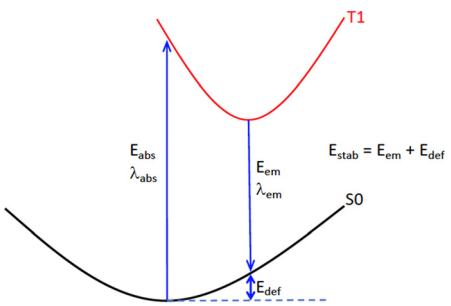

Scheme 3 Definition of the stabilization and deformation energies at the low-lying triplet optimized structures illustrated here for T1.

On the basis of the above-mentioned low-lying triplet state properties only the transitions possessing significant LC_{NHC} contribution are eligible for an intense CPL activity. According to our calculations, two main CPL bands may be observed: the one initiated from T_1 in the 700–750 nm energy domain and a second one originated from T_4 around 650 nm. Both of them possess substantial LC_{NHC} character.

A more refined costly theoretical treatment of the luminescence properties of this series of complexes, as developed in the recent article by Shafei *et al.*[16] based on the deconvolution of the relevant magnetic sub-levels and including vibronic analysis is not proposed here. This is justified by the electronic similarities between the present complexes and the NHC complex of series (**II**), the chiroptical properties of which have been analysed quantitatively.[16] It was shown that the most efficient and fastest emission pathway proceeds through the $M_s = 0$ magnetic sub-level of the parent non-relativistic ground S_0 and T_1, S_2 excited states, mainly of MLCT/XLCT character, creating unpolarized photons. Indeed, the emission activities, both PL and CPL, are governed by the electronic properties (including SOC and vibronic effects) and by the induced magnetic anisotropy arising from coupling between orbital and spin angular momenta. By analogy with the "J–K" coupling mechanism in magnetic circular dichroism (MCD),[25] the right-handed and left-handed photon emission, respectively induced by electric and magnetic dipole allowed $|\pi^* \rightarrow| d_{yz} - p_y$ and $|\pi^* \rightarrow| d_{xz} - p_x$ electron decay associated to the MLCT/XLCT (XLCT/MLCT) states, cancel each other leading to weak CPL signals.

The next sections report on the synthesis, characterization, photophysical and chiroptical properties of the benzannulated NHC rhenium(I) tricarbonyl complexes **1Cl**, **1Br**, **1I**, **2Br-6Br**

 This journal is © the Owner Societies 2024

Published on 14 November 2023. Downloaded on 11/20/2025 6:23:24 PM.

investigated theoretically and discussed above. The last section of the manuscript is dedicated to the experimental protocol and computational details.

2.2. Synthesis

As compared to the reference complexes depicted in Scheme 1 and studied both theoretically[16] and experimentally,[14] the series of molecules investigated here present the following four advantages: (i) much easier synthetic protocol; (ii) large degree of LC_{NHC} character in the lowest triplet states compared to the small NHC compounds of series (**I-II**) (Scheme 1), yet the partial MLCT character ensures faster radiative excited state decay compared to helicenic derivatives,[28] (iii) emission and CPL signals shift bathochromically compared to previously reported NHC–rhenium(I) derivatives; (iv) the problem of steric hindrance induced by helicenic ligands that inhibits the necessary ligand rotation for an optimal magnetic dipole/electric dipole transition vectors is avoided.[16]

In order to explore the effect imparted by different substituents onto the photophysical and chiroptical properties of the family of benzannulated NHC rhenium(I) tricarbonyl complexes, a series of six 2-(pyridin-2-yl)imidazo[1,5-*a*]pyridin-2-ium proligands, namely **L1H-L6H**, was firstly prepared. The synthetic strategy employed a modified version of the three-component picolinaldehyde-amine-formaldehyde coupling procedure previously reported in the literature,[29] and it is displayed in Scheme S1 of the ESI.† Supplementary procedures and chemical characterization including ^{1}H, ^{13}C{^{1}H} NMR, HR-ESI-MS and elemental analysis are provided as supporting material in the ESI.†

Briefly, ligands **L1H-L6H** were prepared straightforwardly by means of a two-step procedure under microwave (MW) heating (60 W). It began from mixing the corresponding amine and paraformaldehyde (1.5 equiv.) in acetonitrile, followed by addition of the picoline derivative (1 equiv.) and a CH_3CN solution of 3 M HCl. Metathesis reaction by dropwise addition of a saturated aqueous solution of a PF_6^- salt provided the desired ligands as crystalline solids in moderate to high yields. Eight NHC rhenium tricarbonyl complexes bearing a bidentate N^C_{NHC} ligand were subsequently prepared, and their chemical structure is displayed in Scheme 2. Derivative **1Cl** and **1Br** were previously reported by some of us.[17] Nevertheless, an alternative and more efficient synthetic strategy is hereafter presented and generalized to afford six novel homologues straightforwardly.

The derivatives *fac*-[ReX(CO)$_3$(**L1-L6**)] (**1Cl-1Br**, **2Br-6Br**), where X is either Cl or Br, were prepared and in a reaction by suspending the corresponding pyridyl pyridoannelated azolium salt as the NHC source **L1H-L6H**, [ReX(CO)$_5$] (1 equiv.) as the rhenium precursor and K_2CO_3 as the base in Ar-flushed xylene for 4 hours at 130 °C under MW heating (see Scheme S2 of the ESI†). After precipitation and flash-filtration on neutral Al_2O_3, the target complexes were obtained as yellow solids of purity suitable for further photophysical investigation in moderate to high yields. At this stage, it is important to point out that solutions of the complexes were air-sensitive, providing brown by-products if left for a few hours under atmospheric condition. On the other hand, no degradation was observed for solid samples and they appeared to be stable for several months under air. The novel iodide complex, namely **1I**, was prepared by a two-step halogen exchange reaction starting from the chloride analogue **1Cl** and employing $AgPF_6$ (1.3 equiv.) as the de-halogenation reagent, followed by addition of an excess of NH_4I solution in methanol (5.3 equiv.) at room temperature under inert atmosphere (see Scheme S3 of the ESI†). The pure **1I** complex was obtained by flash filtration on neutral alumina.

Clear evidence of the Re–C_{NHC} bond formation is provided by the complete disappearance of the pro-carbenic proton at δ = *ca.* 10.1–10.7 ppm as well as by the presence of four downfield resonances in the region δ = 185–200 ppm of the ^{13}C NMR spectrum. These latter are attributable to the three C≡O and the carbenic C atoms. FT-IR spectrum confirmed the formation of the complex with facial arrangement of the three carbonyl ligands.

2.3. Photophysical investigation

2.3.1. Electronic absorption and photoluminescence. Firstly, the optical properties of so-prepared Re(I) complexes as racemic mixture were investigated in dilute (concentration 2×10^{-5} M) acetone solution in both air-equilibrated and degassed condition at room temperature by means of steady-state and time-resolved photophysical techniques. It should be pointed out that complex **1Cl-1Br** were previously investigated in CH_2Cl_2,[17] and their photophysical investigation in acetone will be reported hereafter for the sake of consistency with the whole investigated series of derivatives. The change in the employed solvent has been dictated by the limited solubility of some of the novel derivatives in CH_2Cl_2. The electronic absorption and emission spectra are displayed in Fig. 8 for compound **1Br**, **2Br** and **3Br** and Fig. S24–S25 of the ESI† for all the other investigated complexes herein. In Table 4 are listed the corresponding photophysical data. For all the derivatives, the absorption spectra show rather similar features in agreement with our previous data.[17] Within the optical transparency window of the employed solvent, two bands are present, yet

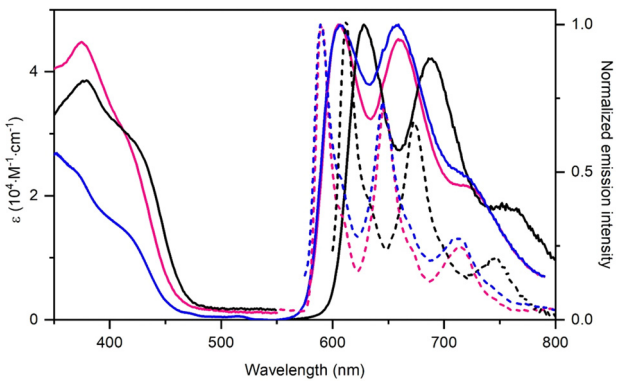

Fig. 8 Electronic absorption and photoluminescence spectra of compounds **1Br** (magenta traces), **2Br** (black traces), and **3Br** (blue traces) in acetone solution at a concentration of 2×10^{-5} M at room temperature (solid line) and 77 K (dashed line) in 2-MeTHF glassy matrix. Emission spectra were recorded upon excitation at λ_{exc} = 400 nm.

Table 4 Photophysical properties of complexes **1–6** in air-equilibrated and degassed acetone solution at a concentration of 2×10^{-5} M at room temperature and at 77 K in 2-MeTHF glassy matrix

Complex	$\lambda_{max,Abs}$ (ε) [nm, (10^3 M^{-1} cm^{-1})]	λ_{em} [nm]	PLQY (%) Air-equilibrated	PLQY (%) Degassed	τ_{obs} Air-equilibrated [ns]	τ_{obs} Degassed [μs]	k_r[a] [10^3 s^{-1}] Degassed	k_{nr}[b] [10^3 s^{-1}] Degassed	λ_{em} 77 K [nm]
1Cl	372 (3.81), 410sh (2.55)	607, 662, 720	<0.1	0.5	153	14.0	0.36	70.9	590, 645, 717
1Br	374 (4.47), 410sh (3.10)	606, 660, 725	0.2	1.7	158	15.4	1.10	63.7	590, 646, 714
1I	382 (4.50), 414sh (3.15)	604, 657, 722	0.2	1.9	149	15.6	1.22	62.7	592, 647, 715
2Br	378 (3.84), 421sh (2.88)	628, 687, 760	<0.1	1.1	117	7.88	1.40	125	612, 673, 745
3Br	412sh (2.39)	606, 657, 721	0.2	2.9	141	19.1	1.51	50.6	591, 646, 714
4Br	370 (4.89), 408sh (3.47)	603, 656, 719	0.2	2.1	151	18.0	1.16	54.1	589, 645, 712
5Br	374sh (2.99), 417sh (2.12)	607, 663, 729	0.1	0.7	95	13.9	0.50	71.3	594, 651, 720
6Br	373sh (3.23), 420sh (2.48)	630, 691, 772	0.1	0.5	5.5	7.04	0.71	141	615, 676, 754

sh denotes a shoulder. [a] k_r = PLQY/τ. [b] k_{nr} = (1 − PLQY)/τ.

Published on 14 November 2023. Downloaded on 11/20/2025 6:23:24 PM.

partially overlapping. The band at $\lambda_{abs,max}$ = 400–420 nm with ε = 2.1–3.4 × 10^3 M^{-1} cm^{-1} that appears as a shoulder can be described as singlet-manifold spin-allowed transition with mixed metal-to-ligand charge transfer (^{1}MLCT) and halogen-to-ligand charge transfer (^{1}XLCT) with overall dπ(Re)p(X) → π^*_{py} character. The ^{1}XLCT is expected to increase in the order **1Cl** to **1Br** to **1I**. The higher energy transition at $\lambda_{abs,max}$ = 370–382 nm can be ascribed to an electronic transition with admixed metal-to-ligand charge transfer and intraligand charge transfer (^{1}MLCT/^{1}ILCT) character (*vide infra*). Little influence on the absorption profile is observed upon halogen variation within the series of complexes **1**, corroborating the theoretical prediction (Fig. 2).

Secondly, the photoluminescence (PL) properties of the complexes were investigated, and the spectra are displayed in Fig. 8 and Fig. S24–S25 of the ESI.† Upon irradiation at λ_{exc}= 380–440 nm, solution samples display a moderate red photoluminescence with a structured profile arising from the ligand-based vibronic progression involving C═N and C═C vibrational modes. Emission spectra appeared to be independent of the nature of the halogen atom as demonstrated by the overlapping profile of compound **1Cl**, **1Br** and **1I** that display very similar emission spectra, peaking at λ_{em} = 606, 660 and 720 nm for complex **1Br** as an example. The calculated emission wavelengths in toluene fall in the same domain, namely from 780 nm to 602 nm (Table 3). On the other hand, methylation at position C1 of the imidazo[1,5-*a*]pyridin-ylidene scaffold yield a bathochromic shift by about 600 cm^{-1} (λ_{em} = 628, 687 and 760 nm for **2Br**, as an example). The introduction of a moderate electron donating group, such as a methyl, on the pyridine scaffold gives rise to minor hypsochromic shift of the emission spectra (*cf.* derivative **1Br** *vs.* **4Br**). These shifts are reproduced theoretically (Table S6 of the ESI†) for the lowest T_1 state that potentially emit at 716 nm (**1Br**) *vs.* 756 nm (**2Br**) *vs.* 710 nm (**4Br**), according to our calculations performed in acetone as solvent.

When going from air-equilibrated to degassed samples an increase of the emission intensity is observed, as shown by the increase of the PLQY value from 0.1–0.2% to 0.5–2.9%, respectively. The two highest values are observed for derivative **3Br** and **4Br** that feature methylated pyridine ligands. Even more remarkably, a sizeable prolongation of the excited-state lifetime is recorded going from of only a few hundreds of nanoseconds up to a few microseconds upon elimination of the quenching dioxygen (see Table 4).

Lowering the temperatures down to 77 K yields to a minor hypsochromic shift by about 400–450 cm^{-1} and retains the highly structured emission profile, as shown by the spectra recorded in frozen samples in 2-MeTHF glassy matrix. Overall, these findings clearly support the mainly triplet-manifold metal-perturbed ligand-centred (^{3}LC) nature with small ^{3}MLCT/^{3}XLCT contribution of the emissive excited state localized onto the bidentate NHC scaffold.

Given the currently growing interest of longer-wavelength emission for potential application in solid-state optoelectronics, in particular when combined with CPL activity, solid-state samples were investigated as neat powder as well and the corresponding emission spectra and data are shown in Fig. S26 and Table S7 of the ESI.† For such samples, similar red and structured emission is retained, yet spectra display a small bathochromic shift compared to fluid solution, but with low PLQY values of *ca.* 1%. On the other hand, the observed shortening of the excited-state lifetime can be attributed to the triplet–triplet annihilation phenomena often observed in long-lived organometallic emitters in solid state.

2.3.2. Chiroptical properties. Highly enantioenriched samples of complexes were successfully obtained by chiral HPLC separation that provided samples with enantiomeric excess (ee) in the range 97–99.5%, except for derivative **6Br**. Experimental details are reported in the ESI.† The chiroptical properties were investigated experimentally by means of ECD and CPL. ECD and CPL spectra were measured in degassed toluene solution at concentration around 10^{-5} M. The spectra recorded for compound **1Cl**, **1Br**, **1I**, **2Br**, **3Br** and **4Br** are depicted in Fig. 9 and the data are listed in Table S8 of the ESI.†

Each enantiomeric pair displays ECD spectra with mirror-image relationship, expectedly. As depicted in Fig. 9, the ECD spectra of all the complexes display similar features. They exhibit a weak negative band λ = *ca.* 353–358 nm ($\Delta\varepsilon$ = −5 to −2 M^{-1} cm^{-1}) and a weak broad positive one at λ = *ca.* 435 nm ($\Delta\varepsilon$ = +2 to +5 M^{-1} cm^{-1}) for the first eluted samples, with the exception of compound **4Br** that corresponds to the second

 This journal is © the Owner Societies 2024

Published on 14 November 2023. Downloaded on 11/20/2025 6:23:24 PM.

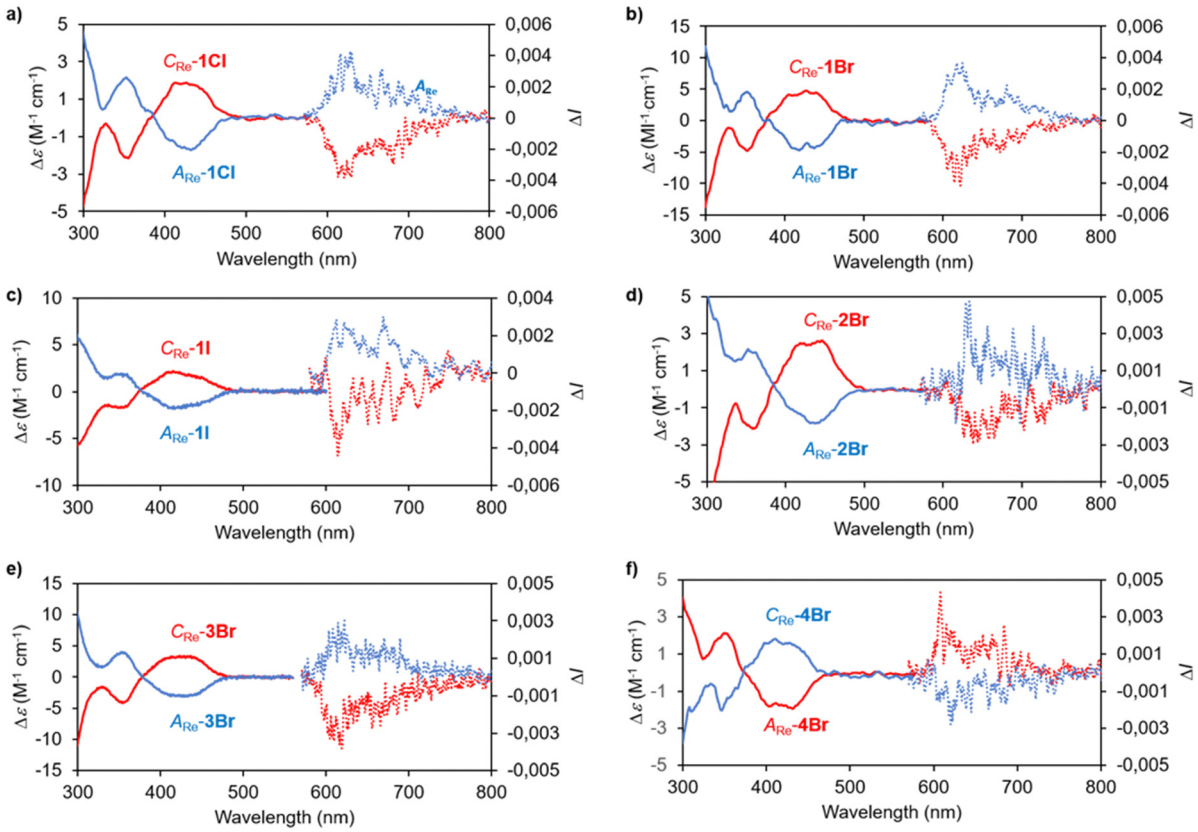

Fig. 9 ECD (solid traces, left) and CPL (dashed traces, right) spectra of enantioenriched C_{Re} and A_{Re} complexes **1Cl** (a), **1Br** (b), **1I** (c), and **2Br-4Br** (d)–(f). The red (blue) color corresponds to the first (second) eluted enantiomer (see ESI†). Emission spectra were recorded upon excitation of the samples at λ_{exc} = 390–395 in toluene.

HPLC eluted sample. Determination of the absolute configuration was based on the computed ECD spectral data and with comparison with already published rhenium complexes.[14] As listed in Table S8 of the ESI,† the g_{abs} values are in the range 0.73–5.5 × 10^{-3}.

Despite the overall weak ECD responses and the moderate PLQY values displayed by this class of chiral-at-metal rhenium complexes, all the investigated derivatives exhibit mirror-image and structured CPL spectra. This strongly suggests that the character of the electronic transitions involved in the lower-lying absorption and emission process is not the same. The rather noisy signals obtained are explained by the moderate quantum yields observed in toluene solution, which required eight scans accumulation to obtain satisfactory spectra. Overall, negative CP phosphorescence were obtained for the first eluted enantiomer, whereas the recorded signal had positive sign for the second eluted one, except for **4Br** (*vide supra*). The sign of the CPL signals is thus found opposite to the lower-energy ECD-active bands, which means that the compounds undergo large electronic reorganization in the excited state prior to emission. This is indeed illustrated by the change of electronic character of the lowest triplet states after nuclear relaxation (Table 3). Nevertheless, for all compounds the g_{lum} values remain constant throughout the emission bands (see the g_{lum} spectra in Fig. S27 of the ESI†) thus suggesting that the radiative de-excitation transition operates from one excited state only. Overall, g_{lum} dissymmetry factors of 3–4 × 10^{-3} were obtained for all complexes in the wavelength range of λ_{em} = 610–630 nm, yielding CPL brightness values, B_{CPL}, in the order of 0.36–1.8 × 10^{-1} (see Table S8 of the ESI†). Compared to previously reported CPL-emissive Re(I) complexes, g_{lum} values for the present investigated complexes are twice as low as those recorded for complex (**III**) in Scheme 1,[14] but remarkably, two- to four-fold higher than those reported for complexes (**I**)–(**II**) and more recently in series (**IV**).[15] The g_{abs} values are overall coherent with previous data, in the 0.5–3 × 10^{-3} range (see Fig. S27 of the ESI†). On the other hand, the overall lower B_{CPL} values are due to the low PLQY that characterize these benzannulated NHC rhenium(I) complexes.

The comparison between the computed (Fig. 4) and experimental (Fig. 9) ECD spectra of **1Cl**, **1Br** and **1I** in toluene illustrates the experimental difficulty at recording highly resolved spectra when handling chiral molecules. However, the broad band centred at 435 nm can be attributed to the electronic transitions observed between 400–500 nm and leading to two maxima at 456/459 nm and 421/429 nm for **1Cl** and **1Br**, respectively and three maxima at 480, 461 and 403 nm for **1I** (Table 1 and Fig. 4). These bands are assigned to transitions of mixed character, the MLCT/XLCT/LC ratio varying along the series as analysed in the theoretical section. A quantitative

Published on 14 November 2023. Downloaded on 11/20/2025 6:23:24 PM.

reproduction of the experimental spectra depicted in Fig. 9 would require the inclusion of spin–vibronic effects[16] as well as a more accurate simulation of the solvent.[28]

3 Experimental section

General considerations

Rhenium pentacarbonyl chloride was purchased from Acros, rhenium pentacarbonyl bromide was purchased from STREM Chemicals. Neutral alumina was purchased from Acros. All syntheses were carried out in an Anton Paar Monowave microwave reactor to ensure homogeneous and controlled heating. Nuclear magnetic resonance spectra were recorded using a Bruker Avance III HD 500 spectrometer equipped with a N_2 cryo-probe CPPBBO Prodigy at 298 K. ^{1}H and ^{13}C{^{1}H} NMR spectra were calibrated to residual solvent signals. J values are given in Hz, where J_o, J_m and J_p indicate coupling constants for *ortho*, *meta* and *para* positions respectively, and J^4 indicate fourth order interactions (Fig. S28–S41 of the ESI†). HR-ESI-MS spectra were recorded on a MicroToF Bruker equipped with an electrospray ionization (ESI) source (Fig. S42–S53 of the ESI†). Infrared spectra were recorded using a Fourier-transformed attenuated total reflectance infrared (FT-ATR-IR) spectrometer from PerkinElmer (Fig. S54 and S55 of the ESI†).

Chiral chromatographic separation

The enantiomers of the NHC rhenium tricarbonyl complexes can be separated by analytical HPLC on chiral stationary phase, using Chiralpak IC, cellulose tris(3,5-dichlorophenylcarbamate), to baseline separate seven of the complexes, and using Chiralpak IG, amylose tris(3-chloro-5-methylphenylcarbamate), for **4Br**. Several milligrams of each enantiomer were isolated by preparative chiral HPLC, except for **6Br**, due to a fast racemization.

Photophysical characterization

Instrument details. Absorption spectra were measured on a Hitachi U-3010 double-beam UV–VIS spectrophotometer and baseline corrected. Steady-state emission spectra were recorded on a Horiba Jobin-Yvon IBH FL-322 Fluorolog 3 spectrometer equipped with a 450 W xenon arc lamp, double-grating excitation, and emission monochromators (2.1 nm mm^{-1} of dispersion; 1200 grooves mm^{-1}) and a Hamamatsu R13456 red sensitive Peltier-cooled PMT detector. Emission and excitation spectra were corrected for source intensity (lamp and grating) and emission spectral response (detector and grating) by standard correction curves. Time-resolved measurements were performed using the time-correlated single-photon counting (TCSPC) electronics option of the TimeHarp 260 board installed on a PicoQuant FluoTime 300 fluorimeter (PicoQuant GmbH, Germany), equipped with a PDL 820 laser pulse driver. A pulsed laser diode LDH-P-C-375 (λ = 375 nm, pulse full width at half maximum FWHM <50 ps, repetition rate 200 kHz–40 MHz) was used to excite the sample and mounted directly on the sample chamber at 90°. The photons were collected by a PMA Hybrid-07 single photon counting detector. The data were acquired by using the commercially available software EasyTau II (PicoQuant GmbH, Germany), while data analysis was performed using the built-in software FluoFit (PicoQuant GmbH, Germany).

Methods

For time resolved measurements, data fitting was performed by employing the maximum likelihood estimation (MLE) methods and the quality of the fit was assessed by inspection of the reduced χ^2 function and of the weighted residuals. For multi-exponential decays, the intensity, namely $I(t)$, has been assumed to decay as the sum of individual single exponential decays (eqn (1)):

$$I(t) = \sum_{i=1}^{n} \alpha_i \exp\left(-\frac{t}{\tau_i}\right) \quad (1)$$

where τ_i are the decay times and α_i are the amplitude of the component at t = 0. In the tables, the percentages to the pre-exponential factors, α_i, are listed upon normalization. Luminescence quantum yields were measured in optically dilute solutions (optical density <0.1 at the excitation wavelength). For solution samples, luminescence quantum yields were measured in optically dilute solutions (optical density <0.1 at the excitation wavelength) and compared to reference emitter by following the method of Demas and Crosby.[30] The Ru(bpy)$_3$Cl$_2$ complex in air-equilibrated water solution at room temperature was used as reference (PLQY = 0.04).[31] For solid state and thin-film samples, the absolute photoluminescence quantum yields (PLQY) were measured on a Hamamatsu Quantaurus-QY C11347-11 integrating sphere upon excitation at λ_{exc} = 320 nm. All the solvents were spectrophotometric grade. Deaerated samples were prepared by the freeze–pump–thaw technique by using a home-made quartz cuvette equipped with a Rotaflo stopcock.

Electronic circular dichroism

Electronic circular dichroism (in M^{-1} cm^{-1}) was measured on a Jasco J-815 Circular Dichroism Spectrometer IFR140 facility, using the PRISM core (Biogenouest©, UMS Biosit, Université de Rennes 1 – Campus de Villejean-35043 Rennes Cedex, France). The concentrations of the samples were measured precisely at *ca.* 10^{-5} M.

Circularly polarized luminescence

Circularly polarized luminescence (CPL) measurements were performed using a home-built CPL spectrofluoropolarimeter (constructed with the help of the JASCO Company). The samples were excited using a 90° geometry with a 150 W LS xenon ozone-free lamp. The concentrations of the samples were measured precisely at *ca.* 10^{-5} M in toluene.

CPL brightness, namely B_{CPL}, was estimated by using the following equation (eqn (2)):[32]

$$B_{CPL} = \left|\frac{1}{2} \times \in (360\ \text{nm}) \times \text{PLQY} \times g_{lum}\right| \quad (2)$$

Computational details

All enantiomeric structures of complexes **1Cl**, **1Br**, **1I**, **2Br-6Br** and **2I-6I** (Scheme 2) were optimized at the density functional theory (DFT/B3LYP)[33] and time dependent DFT (TD-DFT)

 This journal is © the Owner Societies 2024

Published on 14 November 2023. Downloaded on 11/20/2025 6:23:24 PM.

including perturbative spin–orbit effects.[34] levels for the electronic ground state S_0 and low-lying S_1, T_1 and T_2 excited states, respectively. The calculations were based on triple-ζ polarized basis sets[35] including scalar relativistic effects. The Tamm–Dancoff approximation (TDA)[36] was applied to compute the excitation energies. The calculations have been performed in toluene and acetone within the COSMO (conductor-like-screening model) model.[37] The absorption spectra have been computed at the TD-DFT level (80 roots) including spin–orbit effects at the perturbation level of theory within the zero-order relativistic approximation (ZORA)[38] as implemented in ADF-2019 quantum chemistry software.[39] The composition of the excited states has been analysed by means of TheoDORE software.[40] The ECD spectra and associated rotatory strengths were calculated on the basis of time-dependent first-order electric and magnetic properties obtained by means of the linear response of the Kohn–Sham density matrix.[41] The present computational strategy has been validated by previous in-depth theoretical investigation of the optical and photoluminescent spectra of similar chiral Re(I) complexes.[16] TD-DFT/B3LYP/SOC has been compared to TD-DFT/PBE0/SOC and STEOM-DLPNO-CCSD/SOC. Average MAE's from the experimental spectra never exceed 0.18 (ABS) and 0.30 (ECD) at the TD-DFT level and amount to 0.10 (ABS) and 0.09 (ECD) (CCSD/SOC).

4 Conclusion

A novel series of photoactive halo-rhenium(I) tricarbonyl complexes bearing a (substituted) pyridyl benzannulated N-heterocyclic carbenic ligand as π-accepting chromophore is prepared and investigated both as racemic and enantiopure chiral-at-metal species. The compounds display long-lived and structured red phosphorescence arising from an excited-state with ^{3}LC/^{3}MLCT/^{3}XLCT character whose degree of admixing is finely tuned by both substitution on the pyridyl benzannulated–NHC and the ancillary halogen ligand. In-depth computational investigation of both enantiomeric configurations for all the complexes has been performed. The change in character and position of the low-lying electronic excited states induced by substituents, halide, SOC and solvent effects and their consequences on the absorption and ECD spectra have been carefully analysed. It has been shown that stronger ECD signal is provided by transitions with larger LC character as illustrated for the iodo complexes when substituting the pyridyl moiety. Polar solvents such as acetone seem to induce significant hypsochromic shift of the optical spectra and large rotatory strengths while SOC effects lead to batochromic shift *via* singlet/triplet mixing of the low-lying absorbing states. As confirmed experimentally, the potentially luminescent low-lying triplet states undergo important electronic reorganization upon nuclear relaxation. Finally, experimental chiroptical properties for samples in solution show that all the investigated complexes display similar features in both ECD and CPL spectra and $|g_{lum}|$ up to 4×10^{-3} are achieved. Interestingly, opposite sign is recorded for CPL signal compared to the lowest-lying ECD band, indicative of a change of the electronic nature of the involved transitions, as also confirmed by computational investigation. Although $|g_{lum}|$ values are still moderate, they are only two-fold lower than those reported for related helicenic–NHC Re(I) derivatives and two-to-four-fold higher than those observed for smaller NHC-based Re(I) complexes with ^{3}MLCT character of the excited state, highlighting the important role exerted by the partial LC nature (amongst others) of the emissive excited state for achieving CPL emission. The complexes investigated here follow a multistate intensity mechanism similar to the one proposed for other non-helicenic small Re(I)–NHC complexes related to Serie I.[16] This mechanism is controlled by the electronic nature of the emitting excited state multiplet and by its induced magnetic anisotropy.[16] The electric and magnetic transition dipole moments, their degree of forbiddenness and their relative orientation, the spin–orbit and degeneracy effects are all factors that together contribute to the intensity and sign of the circularly polarized luminescence. Within the non-relativistic limit, emitting states of low intensity are x and y polarized electric and magnetic dipole allowed with pronounced MLCT/XLCT character. The electric and magnetic dipole moments oppose each other lowering the intensity. Pure degenerate emitting states may cancel out the CPL signal.

In helicenic Re(I)–NHC complexes characterized by nearly pure LC emitting states the structural properties drive the multistate intensity mechanism. In the case of parallel alignment of the halogen X and helicene ligand the LC emission process involves mainly x and z (Re–X bond orientation) polarized electric and magnetic dipole electron decay leading to nearly orthogonal dipole vectors. Moreover, the rotation of the magnetic induced moment is blocked by steric effects. This results in a negligible rotatory strength and weak CPL intensity similar to the one observed for non-helicenic Re(I)–NHC complexes. Substitution of the halide axial ligand by a less bulky ligand (from I to Cl) attenuates the magnetic blocking and induces a small increase in intensity. In the case of sterically free anti-parallel aligned halogen/helicenic enantiomers the rotation of the magnetic induced moment is free. The LC emission process involved x, y, z polarized electric and magnetic dipole electron decay with a favorable orientation of the dipole vectors leading to an intensity that is three times higher in comparison to the non-helicenic and to the "parallel" variant of the helicenic complexes. The partial LC character of the emitting state of the complexes investigated here explains their intermediate but promising g_{lum} values.

This work will help to shed a better light on the interplay between chemical and electronic structure and chiroptical properties for designing more efficient CPL emitters with potential applications for instance as optoelectronic and bio-imaging molecular materials.

Author contributions

M. D.-P. and J. C. measured the chiroptical properties, analysed the results and wrote the corresponding part of the manuscript

Published on 14 November 2023. Downloaded on 11/20/2025 6:23:24 PM.

and ESI;† N. V. performed and analyzed chiral HPLC separations; V. G. performed the synthesis of the compounds and the photophysics; T. G. has been involved in the computational tasks; M. M. contributions are the conceptualization, photophysics, analysis, supervision, writing and funding acquisition; C. G. contributions are the funding acquisition, project administration, conceptualization, computation, analysis and writing; C. D. has been involved in the conceptualization, modelling and interpretation, analysis, methodology and writing.

Conflicts of interest

There are no conflicts to declare.

Acknowledgements

The Université de Strasbourg and the CNRS are kindly acknowledged for financial support. M. M. gratefully acknowledges the French Agence Nationale de Recherche (ANR) for funding the grants ANR-20-CE29-0021 "PhotoMecha" and ANR-21-CE29-0015 "ChirON". V. G. thanks the College Doctoral of the Université de Strasbourg for partially funding his PhD fellowship. Robin Fleischel of the UFR de Mathématique et d'Informatique of the Université de Strasbourg is kindly acknowledged for help with coding and data processing. The spiral arrow in the graphical abstract is adapted from an illustration by Iñaki Otsoa under CC BY-SA 4.0 Creative Commons license. The calculations have been performed at the HPC, University of Strasbourg, through a grant of computer time.

References

1 G. Albano, G. Pescitelli and L. Di Bari, *Chem. Rev.*, 2020, **120**, 10145–10243.
2 J. Kumar, T. Nakashima and T. Kawai, *J. Phys. Chem. Lett.*, 2015, **6**, 3445–3452.
3 H. Tanaka, Y. Inoue and T. Mori, *ChemPhotoChem*, 2018, **2**, 386–402.
4 H. Tanaka, M. Ikenosako, Y. Kato, M. Fujiki, Y. Inoue and T. Mori, *Commun. Chem.*, 2018, **1**, 38.
5 D.-W. Zhang, M. Li and C.-F. Chen, *Chem. Soc. Rev.*, 2020, **49**, 1331–1343.
6 J. R. Brandt, F. Salerno and M. J. Fuchter, *Nat. Rev. Chem.*, 2017, **1**, 45.
7 J. Gong and X. Zhang, *Coord. Chem. Rev.*, 2022, **453**, 214329.
8 B. Doistau, J.-R. Jiménez and C. Piquet, *Front. Chem.*, 2020, **8**, 555–559.
9 T. J. Penfold, E. Gindensperger, C. Daniel and C. M. Marian, *Chem. Rev.*, 2018, **118**, 6975–7025.
10 D. Bourissou, O. Guerret, F. P. Gabbai and G. Bertrand, *Chem. Rev.*, 2000, **100**, 39–91.
11 *N-Heterocyclic Carbenes: From Laboratory Curiosities to Efficient Synthetic Tools*, ed. S. Díez-González, RSC, Cambridge, UK, 2011.
12 M. N. Hopkinson, C. Richter, M. Schedler and F. Glorius, *Nature*, 2014, **510**, 485–496.
13 For a recent review see: A. Bonfiglio and M. Mauro, *Eur. J. Inorg. Chem.*, 2020, 3427–3442.
14 E. S. Gauthier, L. Abella, N. Hellou, B. Darquié, E. Caytan, T. Roisnel, N. Vanthuyne, L. Favereau, M. Srebro-Hooper, J. A. G. Williams, J. Autschbach and J. Crassous, *Angew. Chem., Int. Ed.*, 2020, **59**, 8394–8400.
15 E. S. Gauthier, L. Abella, E. Caytan, T. Roisnel, N. Vanthuyne, L. Favereau, M. Srebro-Hooper, J. A. G. Williams, J. Autschbach and J. Crassous, *Chem. – Eur. J.*, 2023, **29**, e202203477.
16 R. Shafei, A. Hamano, C. Gourlaouen, D. Maganas, K. Takano, C. Daniel and F. Neese, *J. Chem. Phys.*, 2023, **159**, 084102.
17 A. Bonfiglio, K. Magra, C. Cebrián, F. Polo, P. C. Gros, P. Mercandelli and M. Mauro, *Dalton Trans.*, 2020, **49**, 3102–3111.
18 M. Mauro, E. Quartapelle Procopio, Y. Sun, C.-H. Chien, D. Donghi, M. Panigati, P. Mercandelli, P. Mussini, G. D'Alfonso and L. De Cola, *Adv. Funct. Mater.*, 2009, **19**, 2607–2614.
19 E. Quartapelle Procopio, M. Mauro, M. Panigati, D. Donghi, P. Mercandelli, A. Sironi, G. D'Alfonso and L. De Cola, *J. Am. Chem. Soc.*, 2010, **132**, 14397–14399.
20 M. Mauro, C.-H. Yang, C.-Y. Shin, M. Panigati, C.-H. Chang, G. D'Alfonso and L. De Cola, *Adv. Mater.*, 2012, **24**, 2054–2058.
21 A. Bonfiglio, P.-W. Hsiao, Y. Chen, C. Gourlaouen, Q. Marchand, V. César, S. Bellemin-Laponnaz, Y.-X. Wang, C.-W. Lu, C. Daniel, F. Polo, H.-C. Su and M. Mauro, *Chem. Mater.*, 2022, **34**, 1756–1769.
22 A. Bonfiglio, L. Pallova, V. César, C. Gourlaouen, S. Bellemin-Laponnaz, C. Daniel, F. Polo and M. Mauro, *Chem. – Eur. J.*, 2020, **26**, 11751–11766.
23 P. Ai, M. Mauro, L. De Cola, A. A. Danopoulos and P. Braunstein, *Angew. Chem., Int. Ed.*, 2016, **55**, 3338–3341.
24 N. Darmawan, C.-H. Yang, M. Mauro, M. Raynal, S. Heun, J. pan, H. Buchholz, P. Braunstein and L. De Cola, *Inorg. Chem.*, 2013, **52**, 10756–10765.
25 F. Neese and E. I. Solomon, *Inorg. Chem.*, 1999, **38**, 1847–1865.
26 H. Yersin, A. F. Rausch, R. Czerwieniec, T. Hofbeck and T. Fischer, *Coord. Chem. Rev.*, 2011, **255**, 2622–2652.
27 S. Mandal and C. Daniel, *Phys. Chem. Chem. Phys.*, 2023, **25**, 18720–18727.
28 Q. Yang, M. Fusè, G. Bloino and V. Barone, *Spectrochim. Acta*, 2021, **254**, 119631.
29 J. T. Hutt and Z. D. Aron, *Org. Lett.*, 2011, **13**, 5256–5259.
30 G. A. Crosby and J. N. C. Demas, *J. Am. Chem. Soc.*, 1970, **92**, 7262–7270.
31 I. Ishida, S. Tobita, Y. Hasegawa, R. Katoh and K. Nozaki, *Coord. Chem. Rev.*, 2010, **254**, 2449–2458.
32 L. Arrico, L. Di Bari and F. Zinna, *Chem. – Eur. J.*, 2021, **27**, 2920–2934.
33 P. J. Stephens, F. J. Devlin, C. F. Chabalowski and M. J. Frisch, *J. Phys. Chem.*, 1994, **98**, 11623–11627.
34 F. Wang and T. J. Ziegler, *Chem. Phys.*, 2005, **123**, 154102; F. Wang, T. J. Ziegler, E. van Lenthe, S. van Gisbergen and E. J. Baerends, *J. Chem. Phys.*, 2005, **122**, 204103.
35 E. van Lenthe and E. J. Baerends, *J. Comput. Chem.*, 2003, **24**, 1142–1156.

 This journal is © the Owner Societies 2024

36 M. J. G. Peach and D. J. Tozer, *J. Phys. Chem. A*, 2012, **116**, 9783–9789.
37 A. Klamt, *J. Phys. Chem.*, 1995, **99**, 2224–2235.
38 E. van Lenthe, R. van Leeuwen, E. J. Baerends and J. G. Snijders, *Int. J. Quantum Chem.*, 1996, **57**, 281–293.
39 G. te Velde, F. M. Bickelhaupt, E. J. Baerends, C. Fonseca Guerra, S. J. A. van Gisbergen, J. G. Snijders and T. Ziegler, *J. Comput. Chem.*, 2001, **22**, 931–967. ADF 2019.3, SCM, Theoretical Chemistry, Vrije Universiteit, Amsterdam, The Netherlands, https://www.scm.com.
40 F. Plasser, *J. Chem. Phys.*, 2020, **152**, 084108.
41 J. Autschbach, T. Ziegler, S. J. A. van Gisbergen and E. J. Baerends, *J. Chem. Phys.*, 2002, **116**, 6930–6940; J. Autschbach and T. Ziegler, *J. Chem. Phys.*, 2002, **116**, 891–896.

Published on 14 November 2023. Downloaded on 11/20/2025 6:23:24 PM.